Title
A Novel Method for Repeatable Failure Testing of Annulus Fibrosus

Journal
Journal of Biomechanical Engineering, 139(11)

ISSN
0148-0731

Authors
Werbner, Benjamin
Zhou, Minhao
O'Connell, Grace

Publication Date
2017-11-01

DOI
10.1115/1.4037855

Peer reviewed

A Novel Method for Repeatable Failure Testing of Annulus Fibrosus

Benjamin Werbner
Mechanical Engineering Department,
University of California, Berkeley,
2162 Etcheverry Hall, #1740,
Berkeley, CA 94720-1740
e-mail: benwerbner@berkeley.edu

Minhao Zhou
Mechanical Engineering Department,
University of California, Berkeley,
2162 Etcheverry Hall, #1740,
Berkeley, CA 94720-1740
e-mail: minhao.zhou@berkeley.edu

Grace O'Connell[1]
Mechanical Engineering Department,
University of California, Berkeley,
5122 Etcheverry Hall, #1740,
Berkeley, CA 94720-1740
e-mail: g.oconnell@berkeley.edu

Tears in the annulus fibrosus (AF) of the intervertebral disk can result in disk herniation and progressive degeneration. Understanding AF failure mechanics is important as research moves toward developing biological repair strategies for herniated disks. Unfortunately, failure mechanics of fiber-reinforced tissues, particularly tissues with fibers oriented off-axis from the applied load, is not well understood, partly due to the high variability in reported mechanical properties and a lack of standard techniques ensuring repeatable failure behavior. Therefore, the objective of this study was to investigate the effectiveness of midlength (ML) notch geometries in producing repeatable and consistent tissue failure within the gauge region of AF mechanical test specimens. Finite element models (FEMs) representing several notch geometries were created to predict the location of bulk tissue failure using a local strain-based criterion. FEM results were validated by experimentally testing a subset of the modeled specimen geometries. Mechanical testing data agreed with model predictions (~90% agreement), validating the model's predictive power. Two of the modified dog-bone geometries ("half" and "quarter") effectively ensured tissue failure at the ML for specimens oriented along the circumferential-radial and circumferential-axial directions. The variance of measured mechanical properties was significantly lower for notched samples that failed at the ML, suggesting that ML notch geometries result in more consistent and reliable data. In addition, the approach developed in this study provides a framework for evaluating failure properties of other fiber-reinforced tissues, such as tendons and meniscus.
[DOI: 10.1115/1.4037855]

Introduction

Fiber-reinforced tissues of the musculoskeletal system, such as the annulus fibrosus (AF) in the intervertebral disk, experience large, complex loads during daily activities. Repetitive or excessive loading of these tissues may initiate structural damage and lead to mechanical failure, causing debilitating pain and reduced mobility [1–3]. Understanding failure mechanisms of tissues with limited self-healing capabilities is of particular importance as the increase in AF tears with age may cause a cascade of damage and degeneration [4,5]. For example, AF failure can lead to disk herniation, where prolapse of the nucleus pulposus may impinge on the spinal nerves, causing back and leg pain [6,7].

A comprehensive understanding of soft tissue failure mechanics is important for developing strategies for repairing fiber-reinforced tissues [7,8]. Unfortunately, failure mechanics of fiber-reinforced soft tissues is not yet well understood. For example, the significant variability in AF failure properties reported in the literature makes it difficult to interpret and compare experimental results [9–12]. This in turn makes design and validation of tissue-repair strategies more difficult. Previous studies have shown that this large variability may be due to limitations in specimen size and premature tissue failure near the testing grips [9,11,13]. In particular, tissue failure near the gripped regions, resulting from undesirable stress and strain concentrations near the testing grips [14,15], may yield inconsistent and unreliable failure properties, which do not reflect the true properties of the tissue [14,16]. Recent work by Peloquin et al. identified five different modes of failure in meniscus specimens, with less than 25% of failures occurring at the specimen midlength (ML) [16]. Furthermore, previous investigators have excluded up to 60% of AF samples due to failure near the gripped region, indicating the inefficient use of limited tissue resources [11,12,17].

Repeatable and predictable failure in a test specimen is largely based on the specimen geometry. American Society for Testing and Materials guidelines for testing the strength of materials suggest using dog-bone shaped specimens to ensure that failure occurs away from the testing grips (i.e., midlength failure) [18,19]. Rectangular and dog-bone shaped specimens have been successful in evaluating failure mechanics of tendons and ligaments, where collagen fibers are aligned along the loading direction [20–22]. However, materials with fibers oriented off-axis from the applied loading direction, such as AF (fiber orientation range = 30–45 deg), often fail unpredictably, even with a dog-bone shaped geometry [11,16,23].

Finite element models (FEMs) can provide predictions of stress–strain distributions in complex, fiber-reinforced tissues, which may be difficult or impossible to measure experimentally [24]. For this reason, FEMs are valuable tools for directing and guiding experimental studies. For example, FEMs have been used to evaluate the effect of various gripping techniques for soft tissue mechanics under biaxial tension [15,25]. Conclusions from these models, however, suggested the use of tissue specimen sizes that are not feasible for AF specimens [26]. In particular, the maximum width of test specimens from the AF when testing in the fiber-direction is limited anatomically by the disk height, which is highly species-dependent (e.g., disk heights: rat ~1 mm, bovine ~7 mm, and human ~10 mm) [13,27,28]. However, a certain minimum specimen width is also required to ensure collagen fiber engagement during loading [10,29,30]. These restrictions have resulted in rectangular specimens being widely used to determine uniaxial tensile mechanics of the AF, as the rectangular geometry preserves the limited midlength width [10,29,31,32]. With these experimental design restrictions in mind, we employed FEMs to evaluate the effect of different test specimen geometries on stress and strain distribution prior to performing time- and cost-intensive experiments.

Therefore, the objective of this study was to develop and validate a robust testing protocol for investigating AF failure mechanics, using both computational and experimental methods. In

[1]Corresponding author.
Manuscript received April 28, 2017; final manuscript received September 1, 2017; published online September 27, 2017. Assoc. Editor: Kyle Allen.

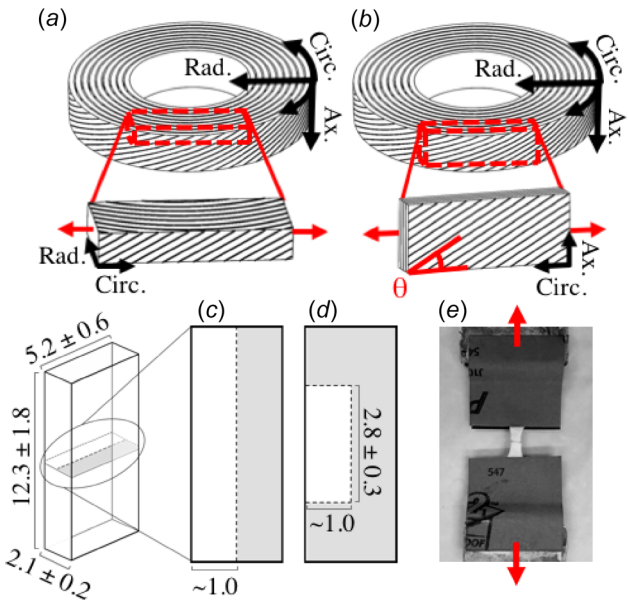

Fig. 1 Schematic of (*a*) circumferential-radial and (*b*) circumferential-axial specimen orientations. Schematic of (*c*) half and (*d*) quarter notch geometries with dimensions given for experimental specimens. Model was created at 40% of experimental dimensions. (*e*) Quarter notch sample glued into sandpaper grips for mechanical testing.

particular, we created several finite element models of AF test specimens using preliminary uniaxial tensile data. Then, we applied the model to investigate local tissue strains and predict the location of bulk tissue failure initiation for various specimen geometries. Finally, we validated the predictive power of the FEM by experimentally testing a subset of the modeled specimen geometries. The method developed in this study mimicked a modified dog-bone geometry at the midsubstance to ensure repeatable failure away from the testing grips. While this technique was developed to evaluate AF failure mechanics, which has fibers oriented off-axis from the primary loading direction, the techniques used here can be widely applied to other soft fiber-reinforced materials.

Materials and Methods

Computational Modeling. Finite element models were developed in FEBio to represent rectangular, uniaxial test specimens oriented in the circumferential-radial (circ.-rad.) and circumferential-axial (circ.-ax.) directions of the AF (Figs. 1(*a*) and 1(*b*)); PreView 1.19.0; FEBio 2.5.2, ~180k nodes and 170k hexahedral elements). Rectangular specimens were modeled at a 2:5 scale of the experimental specimens, where model dimensions were 4.8 mm × 2 mm × 0.8 mm and experimental dimensions were approximately 12 mm × 5 mm × 2 mm for length × width × thickness, respectively. Lamella dimensions were modeled based on values reported for the outer AF (lamella thickness ~200 μm) [23,33]. Circumferential-radial models included ten welded-interface lamellae spanning the 2 mm sample width, and circumferential-axial models included four welded-interface lamellae spanning the 0.8 mm thickness. Fibers were oriented at ±30 deg to the transverse plane to represent the middle-outer AF [23]. Full-width sandpaper grips were simulated to cover 0.4 mm of the tissue at the top and bottom ends.

The tissue was described as a hyperelastic material. The extrafibrillar matrix was modeled using the Mooney–Rivlin description

$$\psi = C_1(\tilde{I}_1 - 3) + C_2(\tilde{I}_2 - 3) + \frac{1}{2}K(\ln J)$$

where C_1 and C_2 are the Mooney–Rivlin material parameters and K represents the bulk modulus ($C_1 = 0.1$ MPa, $C_2 = 0.1$ MPa, and $K = 50$ MPa) [34]. $\tilde{I}_1$ and $\tilde{I}_2$ are the first and second invariants of the deviatoric right Cauchy–Green deformation tensor, respectively, $\tilde{C}(\tilde{C} = \tilde{F}^T\tilde{F})$ and J is the determinant of the deformation gradient tensor ($J = \det(\tilde{F})$). Collagen fibers were modeled using an exponential-linear description

$$\psi_n(\lambda_n) = \begin{cases} 0 & \lambda_n < 1 \\ C_3(e^{C_4(I_4-1)^2} - 1) & 1 \le \lambda_n \le \lambda_0 \\ C_3(e^{C_4(I_4-1)^2} - 1) + (C_5 + D)(\lambda_n - \lambda_0) & \lambda_n > \lambda_0 \end{cases}$$

where C_3 and C_4 represent the exponential-linear coefficients and C_5 represents the fiber modulus ($C_3 = 0.02$ MPa, $C_4 = 30.0$, and $C_5 = 25.0$ MPa). The fourth material parameter, D, was described as a function of C_3 and C_4 ($D = 4C_3C_4(I_4 - 1)e^{C_4(I_4-1)^2}$), and was tuned to obtain a smooth exponential-linear transition. The transition stretch between the toe and linear region is represented by λ ($\lambda = 1.15$). Fibers were modeled as being active only in tension [14]. Material coefficients were determined by curve-fitting to preliminary data that evaluated the subfailure mechanical behavior of specimens oriented along the circumferential-radial and circumferential-axial directions.

In this study, full rectangular specimens were considered the control ("intact"). In addition to the intact model, eight additional models were created to represent samples with various notch geometries at the midlength. For the first notch geometry, a 0.04-mm-thick slice of material was removed at the midlength, such that 75% or 50% of the original cross-sectional area remained ("three-quarters" and "half," respectively; Fig. 1(*c*)—half notch shown). For the second notch geometry, the additional material was removed from the remaining width in the half notch model (e.g., Fig. 1(*d*)—"quarter" notch shown). In order to evaluate the effect of varying cross-sectional area on measured mechanical properties, a total of seven notch geometries were created, such that 3/4, 1/2, 3/8, 1/4, 1/6, 1/10, and 1/20 of the original cross-sectional area remained at the midlength.

Simulated loading was applied in two stages. First, 10% compressive strain was applied at the gripped region. Then, uniaxial tension was applied to 40% global engineering strain along the specimen length. Boundary conditions at the grips were fixed to represent no slipping between the grips and the sample surface. All simulations were solved assuming stepwise static equilibrium and no time-transient effects.

To predict failure location from the model simulations, the strains for the nodes located at the midlength and grip-line were sorted in descending order, and the average for each region was calculated as the average local Lagrangian strain of the top 100 nodes. Then, the average strain at the ML was divided by the average strain at the grips to calculate the ML: grip strain ratio. Therefore, a ML: grip strain ratio greater than 1.0 indicates that the average strain was higher at the midlength than at the grip-line. An average local strain of 65% served as the threshold for the initiation of bulk tissue failure, based on preliminary digital image correlation analysis of experimental data. The threshold was used to predict whether failure would occur at the grips or at the midlength.

Bulk tissue stress in the specimen was calculated by averaging the Lagrangian stress of each node in the cross section located 0.66 mm above the midlength. This cross section was chosen to avoid overestimations of stress due to stress concentrations at the notch and grip-line. The linear-region modulus for each simulation was calculated as the slope of the stress-stretch response for strains between 35% and 40%. The linear-region modulus was normalized using the midlength cross-sectional area to compare different notch geometries.

Experimental Testing. Caudal spine sections from skeletally mature bovines (18 months) were acquired from a local abattoir.

Healthy intervertebral disks were dissected from levels C1–C5 of the spine using a scalpel. Rectangular tissue sections oriented along the circumferential-radial ($n = 16$) or circumferential-axial ($n = 25$) directions were isolated from the middle-outer region of the anterior and posterior AF (Figs. 1(*a*) and 1(*b*), respectively). Preliminary work observed no significant differences in mechanical properties between anterior and posterior bovine AF. A freezing stage microtome was used to reduce the specimen thickness to approximately 2 mm and to ensure planar, parallel surfaces. Since disk mechanical properties are known to vary with hydration state [35], all specimens were soaked in 0.15 M phosphate buffered saline overnight at 37 °C before testing. After hydration, all specimens were trimmed using a parallel-block guide and razor blade to ensure uniform width of 5.2 ± 0.6 mm and thickness of 2.1 ± 0.2 mm.

After hydration and trimming, eight intact specimens were prepared in each orientation. Notched samples were prepared by making a full-width notch at the midlength with a scalpel (#11 blade) and a depth-stop, which resulted in a remaining specimen thickness of 1 mm (half, Fig. 1(*c*); $n = 8$ for each orientation). Additional circumferential-axial samples were notched beyond the half notch configuration, such that the effective gauge width was approximately half of the full width (2.8 ± 0.3 mm). This configuration was used to approximate the quarter notch geometry from the model (Fig. 1(*d*); $n = 9$).

To ensure that slipping did not occur at the grips, two 5 cm × 5 cm squares of 400 grit waterproof sandpaper were fixed to each end of a 5 cm × 2 cm × 1 cm (length × width × thickness) aluminum block using cyanoacrylate, with the grit sides of the sandpaper facing each other. Approximately 10% of the gauge length of each sample was then glued between the other ends of the sandpaper, such that a gauge length of 12.3 ± 1.8 mm remained between the grips (Fig. 1(*e*)). The glue was allowed to dry for 10 min, and samples were rehydrated in 0.15 M phosphate buffered saline for 20 min. The aluminum block and sandpaper fixtures were secured to an Instron testing machine (5943, Norwood, MA) using screw-clamp tension grips. The machine was equipped with a custom-built water bath to ensure proper hydration during testing. Slack was removed from the specimen by applying a 0.05 N preload. The cross-head extension was zeroed and the specimen was photographed with a scale bar to measure specimen-specific dimensions prior to testing.

An extension-controlled ramp was applied at a rate of 50 mm/min until failure. Engineering strain was calculated as the change in cross-head displacement divided by the initial gauge length (i.e., grip-to-grip distance). Engineering stress was calculated by dividing the measured force by the initial cross-sectional area at the midlength. The failure stress (σ_f) was defined as the maximum stress, while the failure strain (ε_f) was defined as the strain at which the maximum stress occurred (Fig. 2—star). The toe- and linear-region moduli (E_{toe} and $E_{lin.}$, respectively) were calculated using a bilinear fit to the stress-strain response (Fig. 2; custom linear-regression algorithm, Matlab Mathworks Inc.).

Stresses and strains from the computational model were compared to experimental results. "Repeatability of failure" was quantified by evaluating the coefficient of variation (or simply "variation"), which was defined as the standard deviation divided by the mean. Variation was calculated for toe- and linear-region moduli, failure stress, and global strain at failure, and was used to compare intact, half notch, and quarter notch geometries for circumferential-axial specimens. A one-way ANOVA with a Tukey–Kramer post-hoc analysis was performed on mechanical properties and variation in mechanical properties. A value of $p \leq 0.05$ indicated a significant difference between groups.

Results

Computational Modeling. The stress–strain response from the computational model matched well with the experimental data ($R = 0.99$; Fig. 2—inset). The initial gripping boundary condition resulted in a small initial strain at the midlength, which was "released" during the first 1% of applied strain during uniaxial tension (Fig. 3—dip from 0–1% strain). Average local strains reached 65% at either the midlength or at the grip-line for all simulations.

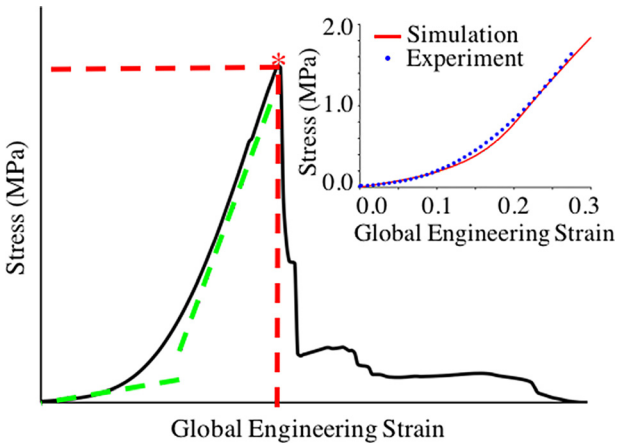

Fig. 2 Representative stress–strain curve. Toe- and linear-region moduli were calculated using a custom linear-regression optimization technique. The point of failure was defined by the maximum stress achieved (star), and this point was used to define the failure stress and failure strain. Inset: computational model fit versus experimental stress–strain curves.

Model simulations predicted grip-line failure for Intact specimens oriented in both the circumferential-radial and circumferential-axial directions (ML:grip ratio < 0.5; Fig. 3; Figs. 4(*a*) and 4(*b*)). For the half notch geometry, the simulations predicted midlength failure for specimens oriented in the circumferential-radial direction (ML:grip ratio ~3.4; Fig. 3; Fig. 4(*c*)) and predicted grip-line failure for specimens oriented in the circumferential-axial direction (ML:grip strain ratio ~0.8; Fig. 3; Fig. 4(*d*)); the grip-line failure for half notch circumferential-axial specimens was predicted with less certainty based on an ML:grip ratio close to 1.0 at predicted failure. For all notch geometries with a midlength cross-sectional area less than 50% of the gripped area (e.g., quarter notch), the ML:grip strain ratio was greater than 1.0 at failure, so midlength failure was predicted (Fig. 3; Fig. 4(*e*)).

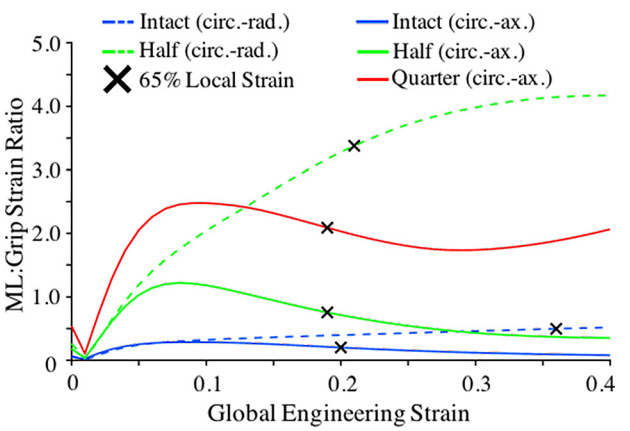

Fig. 3 ML grip strain ratio versus global engineering strain. X's denote predicted failure, which was defined as the point when the average local strain reached 65% at either the ML or the grip-line.

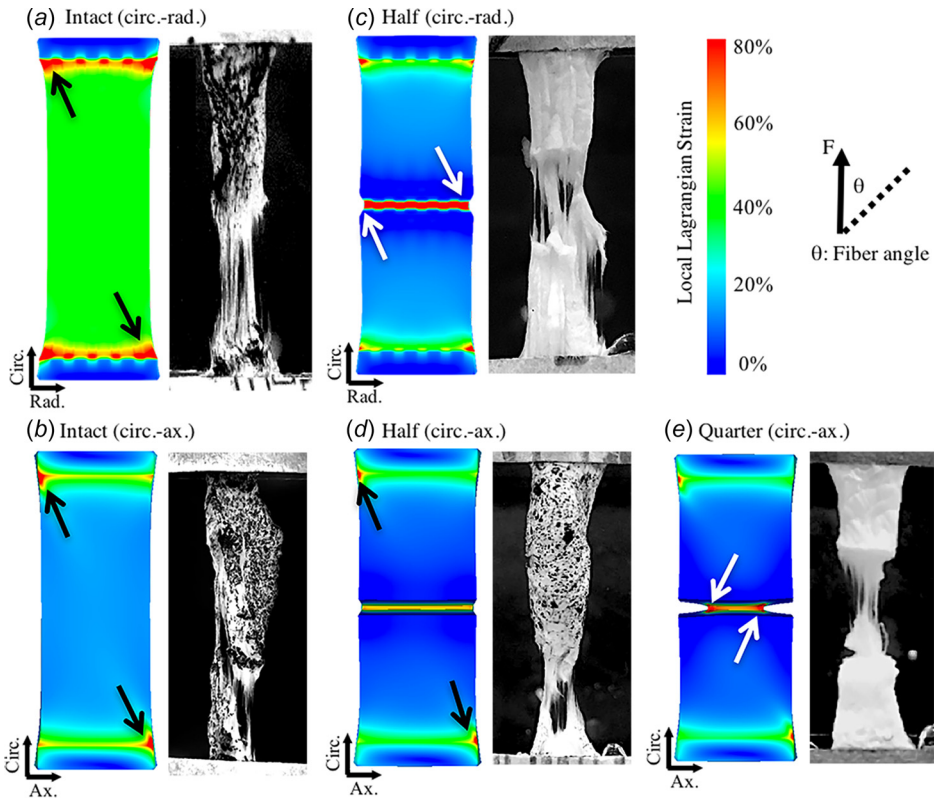

Fig. 4 Strain map at the time-step when failure initiation was predicted by the FEM. Arrows indicate peak local strains. Model simulations in A, B, and D predict bulk tissue failure at the grip-line (black arrows). Model simulations in C and E predict failure at the notch site (white arrows).

The stress–strain response was dependent on the midlength cross-sectional area, where the linear-region modulus decreased as the midlength cross-sectional area increased with respect to the original gripped area (Fig. 5). A similar trend was observed for the failure stress, where samples with a smaller midlength cross-sectional area achieved higher stresses at failure.

Mechanical Testing. All samples tested exhibited a nonlinear stress–strain response (Fig. 2) and no slippage between the sample and testing grips was observed for samples that failed at the midlength. For intact specimens, failure occurred at the grip-line in 100% of circumferential-radial samples ($n = 8/8$; Fig. 4(*a*)) and 88% of circumferential-axial samples ($n = 7/8$; Fig. 4(*b*)). For half notch specimens, failure occurred at the notch site in 100% of circumferential-radial samples ($n = 8/8$; Figs. 4(*c*) and 6), but in only 25% of circumferential-axial samples ($n = 2/8$; Fig. 4(*d*)). Conversely, 90% of quarter notch circumferential-axial specimens failed within 2 mm of the midlength ($n = 8/9$; Fig. 4(*e*)). Failure locations for experimental specimens were consistent with model predictions for all groups (90% agreement; Table 1).

The linear-region modulus and stress at failure for circumferential-radial specimens were approximately half of the values measured for circumferential-axial specimens (Table 2). For circumferential-axial samples, there was a significant decrease in linear-region modulus ($p \leq 0.04$) and failure stress ($p \leq 0.02$) with an increase in midlength cross-sectional area (Figs. 7(*b*) and 7(*c*)). However, there was no significant difference in the toe-region modulus or strain at failure for different notch geometries (Figs. 7(*a*) and 7(*d*)).

The variation of mechanical properties was significantly lower for specimens in which failure occurred at the midlength rather than at the grip line ($p = 0.005$). For example, the coefficient of variation in failure stress was 0.42 (or 42% of the mean) for the

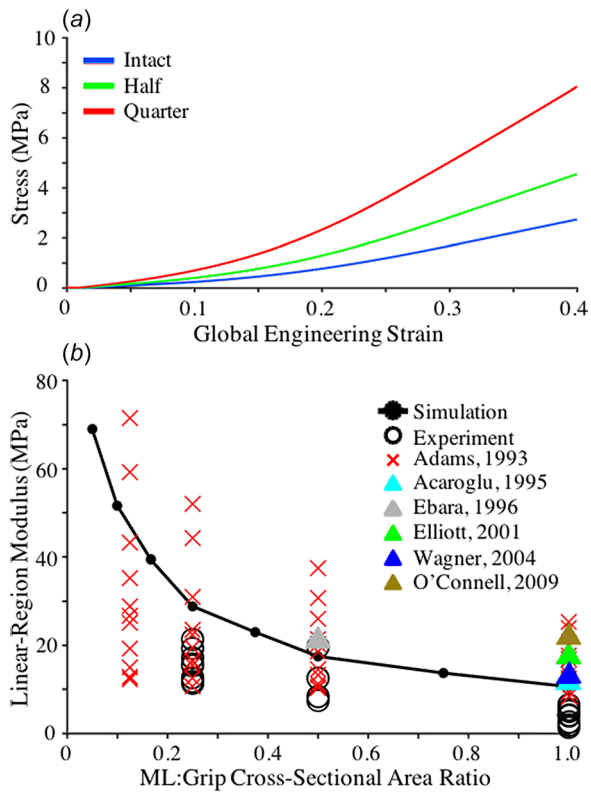

Fig. 5 Simulation results showing the effect of ML cross-sectional area (normalized by gripped area) on (*a*) the stress–strain response and (*b*) the linear-region modulus [9,11,29,36–38]

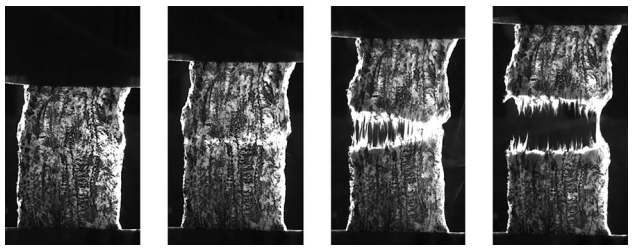

Fig. 6 Representative circumferential-radial sample with a half notch geometry failing at the ML

Table 1 Summary of failure locations for model and experimental specimens. GLF denotes grip-line failure and MLF denotes ML failure for model specimens ("Mod."); the fraction failing at the model-predicted location is given for experimental specimens ("Exp.").

	Intact		Half		Quarter	
	Mod.	Exp.	Mod.	Exp.	Mod.	Exp.
Circ.-Rad.	GLF	8/8	MLF	8/8	N/A	N/A
Circ.-Ax.	GLF	7/8	GLF	6/8	MLF	8/9

Table 2 Measured mechanical properties for experimental specimens failing at the ML

	Circ.-Rad.	Circ.-Ax.
E_{toe} (MPa)	1.39 ± 0.12	1.41 ± 0.07
$E_{lin.}$ (MPa)	8.26 ± 1.66	15.56 ± 3.59
σ_f (MPa)	2.25 ± 0.51	4.67 ± 1.01
ε_f (mm/mm)	0.47 ± 0.07	0.55 ± 0.10

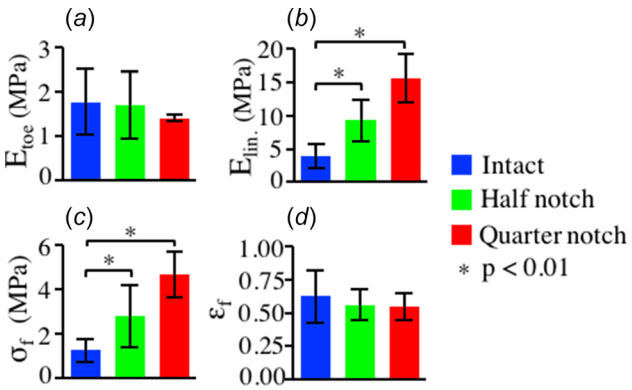

Fig. 7 Mechanical properties of circumferential-axial specimens. Data are reported as the mean plus or minus the standard deviation.

Intact circumferential-axial group and decreased to 0.22 for the quarter notch group (Fig. 8). Similar trends were observed for other mechanical properties (circ.-ax. average variation: intact = 0.41, half = 0.38, and quarter = 0.19; Fig. 8—dashed lines).

Discussion

In this study, we used a combined computational and experimental approach to investigate the effectiveness of several notch geometries for producing repeatable failure of fiber-reinforced tissues. Specifically, we created a finite element model with material

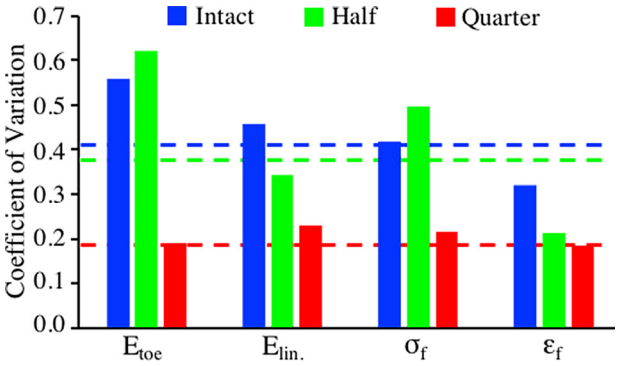

Fig. 8 Coefficient of variation for each measured mechanical property

properties calibrated to preliminary AF tensile data. We used the model to calculate local tissue strains and predict the location of bulk tissue failure. Finally, model predictions were validated experimentally using AF specimens with matching notch geometries. The FEMs used in this study were able to accurately predict failure locations using a local strain-based failure criterion.

Our failure criterion, which defined failure at the midlength when the average local strain there reached 65% before the grip-line, accurately predicted failure at the grips for Intact specimens, regardless of specimen orientation (ML:grip strain ratio = 0.5 and 0.2; Figs. 4(*a*) and 4(*b*)). Mechanical testing data agreed with model predictions, with 94% of intact specimens failing at the grips. Importantly, our model simulations accounted for compressive strains applied at the grips. Model results showed that peak strains at the grip-line were concentrated at the corners, where the longest continuous fibers are likely gripped, suggesting that grip-line failures initiate at the corner of intact specimens.

Adding a simple notch geometry at the midlength of the specimens (half) increased the likelihood of failure; however, this effect was dependent on sample orientation. In circumferential-radial specimens, all half notch samples failed at the notch site, as predicted by the FEM (ML:grip strain ratio at failure∼3.4). However, samples oriented along the circumferential-axial direction required a quarter notch geometry (Fig. 1(*d*)) for predicted failure to occur at the midlength (ML:grip strain ratio = 2.1), which agreed with experimental results (∼90% failures at the notch site). The primary difference between the two sample orientations is the alignment of collagen fibers, where circumferential-axial specimens have longer continuous fibers that are more aligned with the loading direction.

Repeatable midlength failure is essential to ensure accurate material properties and efficient use of limited tissue specimens. Previous studies that investigated failure properties of fiber-reinforced tissues (e.g., AF and meniscus) have reported exclusion of up to 60% of samples from the dataset [9,12,17], due to failure occurring at the grips even when a dog-bone geometry was employed [11,16]. Our model directed us to the half and quarter notch geometries to increase the likelihood of midlength failure for circumferential-radial and circumferential-axial specimens, respectively. Both the half and quarter notch geometries are modified dog-bone geometries that proved effective in ensuring repeatable midlength failure during uniaxial tension. We hypothesize that a combination of failures near the grips and at the midlength likely contributes to the large variability of AF failure data reported in the literature.

Robust failure at the midlength decreased variability in the measured mechanical properties, leading to more accurate characterizations of tissue failure mechanics. The results of this study indicate that specimens failing at the midlength exhibit significantly less variability in their measured mechanical properties. For example, the variation in failure stress for intact samples was

nearly twice that of quarter notch samples (Fig. 8), suggesting that failure properties measured when the sample fails at the midlength are more reliable. Variations in mechanical properties for our notched samples were low compared to values reported in the literature. For example, previously reported coefficients of variation for linear-region modulus, failure stress, and failure strain range from 40 to 100%, 50 to 90%, and 30 to 60%, while our values were limited to approximately 22%, 21%, and 19%, respectively [9–11]. While the notch does create a stress concentration, which may alter measured mechanical properties, previous studies attempting to initiate crack propagation in fiber-reinforced tissues have observed significant blunting at the notch site rather than propagation [16,39,40].

Our results showed a nonlinear increase in linear-region modulus with a decrease in cross-sectional area at the notch site (Figs. 5 and 7(*b*)). This trend is consistent with previous observations in the literature [9,11,17,32,36]. That is, for specimens with a low ML:grip cross sectional area ratio, Young's modulus approached the tensile modulus of the collagen fibers (Fig. 5) [14]. The effect of midlength cross-sectional area on linear-region modulus diminished in samples with a ML:grip cross-sectional area ratio greater than 0.25 [36]. The ML:grip cross-sectional area ratio may be dependent on fiber properties (e.g., orientation and stiffness) [17]. Taken together, these findings suggest that ML:grip cross-sectional area ratios less than 0.25 may result in AF mechanical properties that are not representative of bulk tissue behavior, which includes contributions from the extrafibrillar matrix and fiber-matrix interactions [28,29,38].

Linear-region modulus and failure stress matched well between computational and experimental results (Fig. 5) and were similar to the previously reported values [1,9–11]. While FEM predictions were correct for ~90% of tested samples, the discrepancies between model predictions and experimental results ($n = 4$) may be due to the failure criterion selected. That is, using a higher ML:grip strain ratio may be necessary for better agreement between the model and experimental results (e.g., 2.0 rather than 1.0 used in this study). The predicted failure strain (~20% strain) matched the literature well [1,9,11,41], but was less than half of the experimentally measured failure strain (~50%); this difference is likely due to the model describing the tissue as a hyperelastic material, which cannot account for strain-rate effects. Specifically, failure strain has been reported to increase with applied strain rate [22,42–44], which partly explains the disagreement in failure strains. Moreover, we did not account for the effect of tissue swelling, which is known to alter time-dependent tissue mechanics [35,45]. Furthermore, histological assays were not performed to confirm that the thickness of bovine lamella is equivalent to human lamella, which contribute to the differences observed in model-predicted failure strain and experimental results. Future work will investigate failure mechanics at multiple strain rates and hydration levels to determine the effect of AF structure-function relationship on bulk tissue failure.

This study used a combined approach of computational modeling and mechanical testing to develop and validate a method for sample preparation that ensures repeatable midlength failure in a fiber-reinforced soft tissue. These results indicated that it is essential to consider strains created at the grips during testing to ensure repeatable failure within the gauge region. The methods presented here may facilitate more efficient and accurate evaluation of the failure properties of both native fiber-reinforced tissues and tissue-engineered constructs. Additionally, the homogeneity of the model developed in this study allows it to be scaled for investigating specimens of any size based on tissue availability. In conclusion, the techniques developed here are important for elucidating mechanisms of failure in fiber-reinforced tissues.

Acknowledgment

This work was supported by the Keith L. Markolf - Robert F. Steidel, Jr. Graduate Fellowship and the Hellman Foundation. The authors would like to thank Sam Pliska for his help with mechanical testing.

References

[1] Iatridis, J., MacLean, J., and Ryan, D., 2005, "Mechanical Damage to the Intervertebral Disc Annulus Fibrosus Subjected to Tensile Loading," J. Biomech., **38**(3), pp. 557–565.
[2] Mengoni, M., Jones, A., and Wilcox, R., 2016, "Modelling the Failure Precursor Mechanism of Lamellar Fibrous Tissues, Example of the Annulus Fibrosus," J. Mech. Behav. Biomed. Mater., **63**, pp. 265–272.
[3] CDC, 2005, "Prevalence and Most Common Causes of Disability Among Adults—United States," Morbidity Mortal. Wkly. Rep., **58**(16), pp. 421–426.
[4] Adams, M., and Roughley, P., 2006, "What is Intervertebral Disc Degeneration, and What Causes It?," Spine, **31**(18), pp. 2151–2161.
[5] Vernon-Roberts, B., Moore, R., and Fraser, R., 2007, "The Natural History of Age-Related Disc Degeneration," Spine, **32**(25), pp. 2797–2804.
[6] Weigel, M., Armijos, R., and Beltran, O., 2014, "Musculoskeletal Injury, Functional Disability, and Health-Related Quality of Life in Aging Mexican Immigrant Farmworkers," J. Immigrant Minority Health, **16**(5), pp. 904–13.
[7] O'Connell, G., Leach, K., and Klineberg, E., 2015, "Tissue Engineering a Biological Repair Strategy for Lumbar Disc Herniation," Biores. Open Access, **4**(1), pp. 431–435.
[8] Long, R., Torre, O., Hom, W., Assael, D., and Iatridis, J., 2016, "Design Requirements for Annulus Fibrosus Repair: Review of Forces, Displacements, and Material Properties of the Intervertebral Disk and a Summary of Candidate Hydrogels for Repair," ASME J. Biomech. Eng., **138**(2), p. 021007.
[9] Acaroglu, E., Iatridis, J., Setton, L., Foster, R., Mow, V., and Weidenbaum, M., 1995, "Degeneration and Aging Affect the Tensile Behavior of Human Lumbar Anulus Fibrosus," Spine, **20**(24), pp. 2690–2701.
[10] Green, T., Adams, M., and Dolan, P., 1993, "Tensile Properties of the Annulus Fibrosus," Eur. Spine J., **2**(4), pp. 209–214.
[11] Ebara, S., Iatridis, J., Setton, L., Foster, R., Mow, V., and Weidenbaum, M., 1996, "Tensile Properties of Nondegenerate Human Lumbar Anulus Fibrosus," Spine, **21**(4), pp. 452–461.
[12] Skaggs, D., Weidenbaum, M., Ratcliffe, A., and Mow, V., 1994, "Regional Variation in Tensile Properties and Biochemical Composition of the Human Lumbar Annulus Fibrosus," Spine, **19**(12), pp. 1310–1319.
[13] O'Connell, G., Vresilovic, E., and Elliott, D., 2007, "Comparison of Animals Used in Disc Research to Human Lumbar Disc Geometry," Spine, **32**(3), pp. 328–33.
[14] Holzapfel, G., Schulze-Bauer, C., Feigl, G., and Regitnig, P., 2005, "Single Lamellar Mechanics of the Human Lumbar Anulus Fibrosus," Biomech. Model Mechanobiol., **3**(3), pp. 125–140.
[15] Jacobs, N., Cortes, D., Vresilovic, E., and Elliot, D., 2013, "Biaxial Tension of Fibrous Tissue: Using Finite Element Methods to Address Experimental Challenges Arising From Boundary Conditions and Anisotropy," ASME J. Biomech. Eng., **135**(2), p. 021004.
[16] Peloquin, J., Santare, M., and Elliott, D., 2016, "Advances in Quantification of Meniscus Tensile Mechanics Including Nonlinearity, Yield, and Failure," ASME J. Biomech. Eng., **138**(2), p. 021002.
[17] Lechner, K., Hull, M., and Howell, S., 2000, "Is the Circumferential Tensile Modulus Within a Human Medial Meniscus Affected by the Test Sample Location and Cross-Sectional Area?," J. Orthop. Res., **18**(6), pp. 945–951.
[18] ASTM, 2004, "Standard Test Methods for Tension Testing of Metallic Materials," ASTM, West Conshohocken, PA, Standard No. ASTM E8/E8M-13.
[19] ASTM, 2003, "Standard Test Method for Tensile Properties of Plastics," ASTM International, West Conshohocken, PA, Standard No. ASTM D638-14.
[20] Kolz, C., Suter, T., and Henninger, H., 2015, "Regional Mechanical Properties of the Long Head of the Biceps Tendon," Clin. Biomech., **30**(9), pp. 940–5.
[21] Morales-Orcajo, E., De Bengoa Vallejo, R., Iglesias, M., and Bayod, J., 2016, "Structural and Material Properties of Human Foot Tendons," Clin. Biomech., **37**, pp. 1–6.
[22] Yamamoto, N., and Hayashi, K., 1998, "Mechanical Properties of Rabbit Patellar Tendon at High Strain Rate," Biomed. Mater. Eng., **8**(2), pp. 83–90.
[23] Cassidy, J., Hiltner, A., and Baer, E., 1989, "Hierarchical Structure of the Intervertebral Disc," Connect. Tissue Res., **23**(1), pp. 75–88.
[24] Schmidt, H., Bashkuev, M., Dreischarf, M., Rohlmann, A., Duda, G., Wilke, H., and Shirazi-Adl, A., 2013, "Computational Biomechanics of a Lumbar Motion Segment in Pure and Combined Shear Loads," J. Biomech., **46**(14), pp. 2513–2521.
[25] Sun, W., Sacks, M., and Scott, M., 2005, "Effects of Boundary Conditions on the Estimation of the Planar Biaxial Mechanical Properties of Soft Tissues," ASME J. Biomech. Eng., **127**(4), pp. 709–715.
[26] Waldman, S. D., and Lee, J. M., 2005, "Effect of Sample Geometry on the Apparent Biaxial Mechanical Behavior of Planar Connective Tissues," Biomater., **26**(35), pp. 7504–7513.
[27] Bass, E., Ashford, F., Segal, M., and Lotz, J., 2004, "Biaxial Testing of Human Annulus Fibrosus and Its Implications for a Constitutive Formulation," Ann. Biomed. Eng., **32**(9), pp. 1231–1242.
[28] O'Connell, G., Sen, S., and Elliott, D., 2011, "Human Annulus Fibrosus Material Properties From Biaxial Testing and Constitutive Modeling are Altered With Degeneration," Biomech. Model. Mechanobiol., **11**(3–4), pp. 493–503.
[29] O'Connell, G., Guerin, H., and Elliott, D., 2009, "Theoretical and Uniaxial Experimental Evaluation of Human Annulus Fibrosus Degeneration," ASME J. Biomech. Eng., **131**(11), p. 111007.

[30] Nagel, T., Hadi, M., Claeson, A., Nuckley, D., and Barocas, V., 2014, "Combining Displacement Field and Grip Force Information to Determine Mechanical Properties of Planar Tissue With Complicated Geometry," ASME J. Biomech. Eng., **136**(11), p. 114501.
[31] Guerin, H., and Elliott, D., 2006, "Degeneration Affects the Fiber Reorientation of Human Annulus Fibrosus Under Tensile Load," J. Biomech., **39**(8), pp. 1410–1418.
[32] Wagner, D., Reiser, K., and Lotz, J., 2006, "Glycation Increases Human Annulus Fibrosus Stiffness in Both Experimental Measurements and Theoretical Predictions," J. Biomech., **39**(6), pp. 1021–1029.
[33] Marchand, F., and Ahmed, A. M., 1990, "Investigation of the Laminate Structure of Lumbar Disc Annulus Fibrosus," Spine, **15**(5), pp. 402–410.
[34] Maas, S., Rawlins, D., Weiss, J., and Ateshian, G., 2011, "Febio Theory Manual," Musculoskeletal Research Laboratories, University of Utah, Salt Lake City, UT.
[35] Bezci, S., Nandy, A., and O'Connell, G., 2015, "Effect of Hydration on Healthy Intervertebral Disk Mechanical Stiffness," ASME J. Biomech. Eng., **137**(10), p. 101007.
[36] Adams, M., and Green, T., 1993, "Tensile Properties of the Annulus Fibrosus," Eur. Spine J., **2**(4), pp. 203–208.
[37] Elliott, D., and Setton, L., 2001, "Anisotropic and Inhomogeneous Tensile Behavior of the Human Anulus Fibrosus: Experimental Measurement and Material Model Predictions," ASME J. Biomech. Eng., **123**(3), pp. 256–263.
[38] Wagner, D., and Lotz, J., 2004, "Theoretical Model and Experimental Results for the Nonlinear Elastic Behavior of Human Annulus Fibrosus," J. Orthop. Res., **22**(4), pp. 901–909.
[39] Von Forell, G., Hyoung, P., and Bowden, A., 2014, "Failure Modes and Fracture Toughness in Partially Torn Ligaments and Tendons," J. Mech. Behav. Biomed. Mater., **35**, pp. 77–84.
[40] Taylor, D., OMara, N., Ryan, E., Takaza, M., and Simms, C., 2012, "The Fracture Toughness of Soft Tissues," J. Mech. Behav. Biomed. Mater., **6**, pp. 139–147.
[41] Galante, J., 1967, "Tensile Properties of the Human Lumbar Annulus Fibrosus," Acta. Orthop. Scand., **38**(Sup.100), pp. 1–91.
[42] Noyes, F., DeLucas, J., and Torvik, P., 1974, "Biomechanics of Anterior Cruciate Ligament Failure: An Analysis of Strain-Rate Sensitivity and Mechanisms of Failure in Primates," J. Bone Joint Surg. Am., **56**(2), pp. 236–253.
[43] Crowninshield, R., and Pope, M., 1976, "The Strength and Failure Characteristics of Rat Medial Collateral Ligaments," J. Trauma Acute Care Surg., **16**(2), pp. 99–105.
[44] Woo, S., Peterson, R., Ohland, K., Sites, T., and Danto, M., 1990, "The Effects of Strain Rate on the Properties of the Medial Collateral Ligament in Skeletally Immature and Mature Rabbits: A Biomechanical and Histological Study," J. Orthop. Res., **8**(5), pp. 712–721.
[45] Ateshian, G., Chahine, N., Basalo, I., and Hung, C., 2004, "The Correspondence Between Equilibrium Biphasic and Triphasic Material Properties in Mixture Models of Articular Cartilage," J. Biomech., **37**(3), pp. 391–400.